Invited Paper

Near-field studies of surface plasmon generation: optical and terahertz studies

H. W. Kihm[1], K. G. Lee[1], M. A. Seo[1], K. J. Ahn[1], A. J. L. Adam[2], J. H. Kang[3], Q. H. Park[3], and P. C. M. Planken[2], and D. S. Kim[1+]

[1]Department of Physic and Astronomy, Seoul National University, Seoul 151-747, Korea

[2]University of Technology Delft, Faculty of Applied Sciences, Lorentzweg 1, 2628 CJ Delft, The Netherlands

[3]Department of Physics, Korea University, Seoul 136-701, Korea

[+]dsk@phya.snu.ac.kr

ABSTRACT

We study the dielectric constant dependent diffraction phenomena of single slit apertures, both theoretically and experimentally. We experimentally simulate perfect metal and real metal cases by investigating subwavelength diffraction by a single slit, both in nano-optical and in terahertz regimes, keeping the slit-width/wavelength ratio approximately the same for both of frequency regimes. The wave-front in optical regime separates itself into forward propagating beam and surface-bound 90-degree diffracted wave, i.e., surface plasmon polaritons; while the separation of modes is not observed in terahertz regime.

Keywords: near-field, THz spectroscopy, Surface plasmon.

1. INTRODUCTION

Surface wave propagating on a conducting surface has been a fascinating issue in radio antenna community since Zenneck derived the surface bound wave solution which satisfies Maxwell's equation. Especially, experimental measurement of surface wave excluding diffracted wave which propagates into free space (space wave) has been a crucial problem for those who sought to use this surface wave in radio frequency applications[1].

Surface Zenneck wave in optical and terahertz regime, which is frequently denoted as the surface plasmon polariton (SPP), is also attracting research efforts, because it has a wide range of potential application such as subwavelength focusing[2,3], field amplification[4], or novel biological sensors.

SPP is an interesting topic in both optical frequency and THz frequency regimes; but SPP features are more significant in optical frequency regime than in THz frequency regime. The huge permittivity of metal in THz frequency makes SPP loosely bounded on the surface to lose the advantages of surface bounded wave. To overcome this weakness in THz frequency, some previous researches have reported the mimicking SPP[5] by indenting periodic holes or dimples on flat metal surface. These researches show that SPP behavior is heavily dependent on the frequency and different SPP characteristics in optical and THz frequency regimes.

In these two far separated frequency regimes, the transition of SPP to space wave is an interesting issue, because the discrimination of SPP from space wave is related to noise level in SPP devices.

Here, we address this problem both in experimental and theoretical sides. Near-fields of SPP are measured in nano-optical and terahertz regime, respectively. Between them there are wide wavelength and conductivity gaps. Polarization resolved near-field images in optical and THz frequency regimes provide valuable insights on how SPP and space wave are generated and propagating. By performing finite-difference-time-domain calculations in gap frequency regimes, that is not covered by optical and THz radiation source, the excitation wavelength dependent trends of SPP discrimination from space wave are presented.

Plasmonics: Metallic Nanostructures and Their Optical Properties VI, edited by Mark I. Stockman
Proc. of SPIE Vol. 7032, 70321P, (2008) · 0277-786X/08/$18 · doi: 10.1117/12.794362

2. METHODOLOGY

2.1 Near-field scanning microscope (NSOM) in optical frequency

We use a scattering type NSOM (s-NSOM) to probe an optical near-field. The key idea of a s-NSOM is measuring the scattered light from a NSOM probe apex which extracts the local near-field into the far-field. To improve the scattering efficiency of a NSOM probe, various types of the probe are used, such as an etched metal tip or a metallic nano-particle attached to the probe. In our experiment, we attach a gold nano-particle with diameter of 100 nm onto the tip apex. The fabrication process can be found in elsewhere[7].

Our experimental schematic of an optical s-NSOM is shown in fig. 1. We illuminate a 780 nm wavelength cw-mode Ti:sapphire laser polarized perpendicular to the slit direction. The slit aperture with 200 nm width is perforated on a 150 nm thick gold film with focused ion beam milling process. The gold nano-particle attached probe is raster scanned above the surface, and the scattered signal is collected by a long working distance objective lens (Mitutoyo M Plan Apo 10 x, Japan). We guide the scattered light through a spatial filter with area of few μm^2 to filter out unwanted diffracted light other than from the gold particle. The signal intensity is measured by an avalanche photodiode detector (Hamamatsu C4777-01, Japan) combined with a linear polarizer.

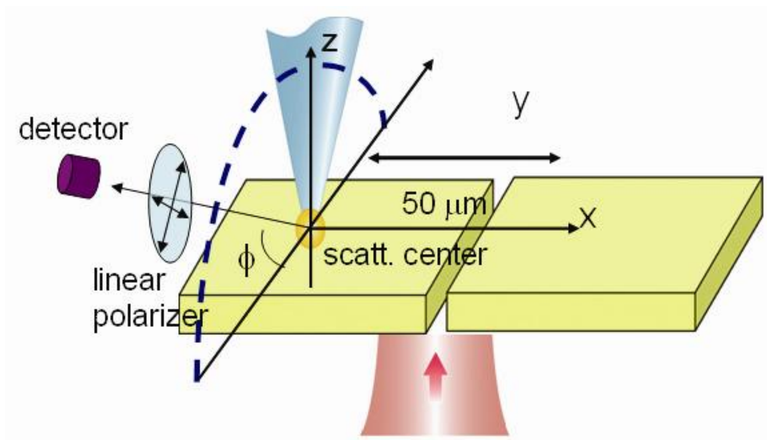

Fig. 1. Experiment schematic of a scattering type NSOM. The diffracted light from the slit aperture and SPP is scattered off at the probe apex into the far-field, and the polarization state of scattered signal is analyzed by rotating the linear polarizer in front of the detector.

We measure the local electric field with polarization analysis of the scattered light. The local electric field induces the polarization $\vec{p}$ on the gold nano-particle with a polarizability α, because the gold nano-particle with a subwavelength size can be treated as an effective dipole scatterer. The scattered light from the particle is carrying information about both the direction and the strength of the local electric field. Thus, we can retrieve the local electric field with prior knowledge about the polarizability α of the gold nano-particle

.

$$\vec{E}_{local} = \overleftrightarrow{\alpha}^{-1} p \quad . \tag{1}$$

The characterization of the polarizability of the gold nano-particle is performed with polarization resolved far-field scattering measurement. We illuminate the 780 nm wavelength laser light at the gold nano-particle attached probe. The incident beam direction is perpendicular to probe axis to determine the x- and z- polarizability components. We measure the scattered signal with the detector positioned in the direction orthogonal to the incident beam path to block out the direct scattered light. By rotating the incident polarization and analyzing the polarization of the scattered light, we can determine the polarizability tensor α which is written as

$$\overleftrightarrow{\alpha} = \begin{pmatrix} \alpha_{xx} & \alpha_{xz} \\ \alpha_{zx} & \alpha_{zz} \end{pmatrix} \quad . \tag{2}$$

For the clarity of polarization analysis, we choose an almost spherical shaped particle whose polarizability tensor can be considered as a nearly-identity matrix.

2.2 Near-field vectorial Fourier Transform 2D microscopy in THz frequency regime

Terahertz time-domain spectroscopy (THz-TDS) is a spectroscopic technique capable of measuring the phase and amplitude of the electric field in an ultra-wide THz bandwidth. In our experiment, we fully utilize THz-TDS to perform the near-field imaging. Fig. 2 shows the schematic of our THz vector microscope. An x-polarized (perpendicular to slit) THz beam is incident on a single slit sample with a width of 60 micron. Around the exit side of the slit, electric field vectors have a strong positional dependence. Each of the vector components of the electric field is detected by using the electro-optic sampling technique in which a THz electric field induces a refractive index change in an electro optic (EO) material at visible-near-IR frequencies that is proportional to the instantaneous field. This refractive index change affects the ellipticity of a circularly polarized light which is focused to a small spot less than 10 micron on the front surface of the EO-crystal using a refractive objective. The probe pulse, reflected from the front surface, is sent to a standard differential detection setup which measures THz field amplitude. The spatial resolution of this technique is limited by the beam spot size of the laser probe beam. Taking account of the wavelength of the excitation THz pulse, we can achieve a $\lambda/30$ resolution. By varying the time delay between the probe pulse and the incident THz pulse, the full electric field as a function of time is obtained. Two differently oriented EO-crystals with a thickness of 300 micron are used. The EO crystal is raster-scanned in the xz-plane with a step size of 20 μ*m* for each pixel, the temporal evolution of the electric field is measured. A Fast Fourier Transform (FFT) of the raster-scanned time traces at every pixel results in images at each frequency component at a zero temporal phase, $\omega t' = 0$ over the entire spectral range, complete with amplitude and phase:

$$\vec{E}(x,0,z,\omega) = \frac{1}{2\pi}\int \vec{E}(x,0,z,t)e^{i\omega t}dt \quad . \tag{3}$$

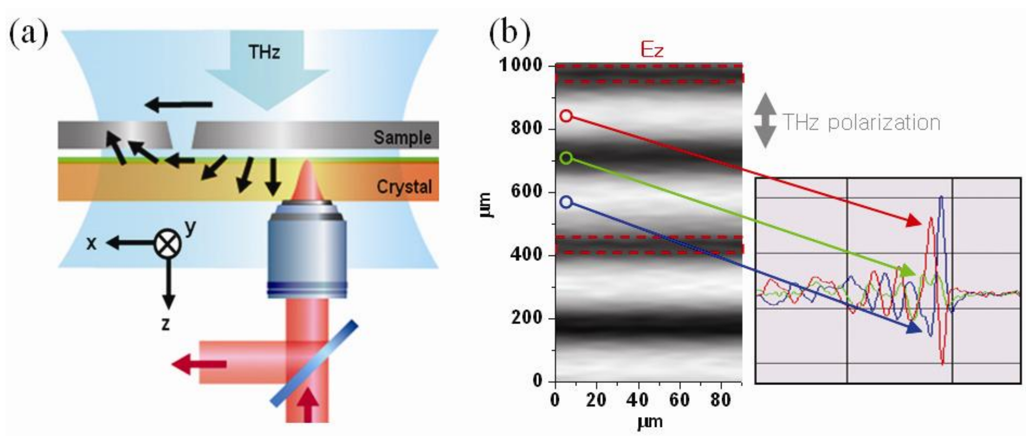

Fig. 2. (a) Schematic of the terahertz near-field microscopy setup. Electro-optic sampling is used to detect the real-time electric field at each position. We raster-scan the sample to obtain data along the *x*-axis, and then move the sample upward. We use two GaP crystals with different crystal oriented along the (110) and (001), respectively to detect the *x*- and *z*- components of the electric field. (b) The near-field of the z-polarized electric field component of a multiple slit sample. The measured THz signal on the slit aperture and a metal surface shows different behavior in time domain. FFT processed on time domain data is converted into frequency domain.

As shown in fig. 2 (b), the near-field of multiple slit is obtained. The left side and the right side of the slit aperture are indicated by a blue arrow and a red arrow respectively. The signals on different spatial regions show clearly different time-domain THz signal with out of phase. These opposite phases in time domain reveals that the phase inversion on different side of the slit aperture dues to its symmetry with respect to the electric field direction.

3. RESULTS AND DISCUSSIONS

In THz regime, we measure the vectorial electric field around the single slit aperture perforated on an aluminum sheet (60 μm of width) using a polarization-resolved THz time-domain imaging[6]. Electro-optic crystals of different orientations provide images of different electric field vector components, and images at each frequency are generated through Fourier-transforming the original time-dependent images. Shown in fig 3. (a) is an intensity $E_x^2 + E_z^2$ plot at an arbitrary temporal phase at frequency 1.2 THz. The emerging wave-fronts from the slit are continuous without a break, without any signature of an apparently surface-bound mode. In optical regime (wavelength=780 nm), we performed vector-field mapping[7] of light emerging from a single nano-slit (width=200 nm) using a gold nano-particle functionalized tip, obtaining a time-averaged intensity $< E_x^2 + E_z^2 >$. In a stark contrast compared to THz regime, upon exiting the slit, the wave-fronts are immediately separated into the propagating and the surface-bound SPP waves. Theoretical results in Fig. 3 (c) and (d) show qualitative agreements with experimental near-field measurements, especially, in terms of the presence of surface-bound waves in the optical regime.

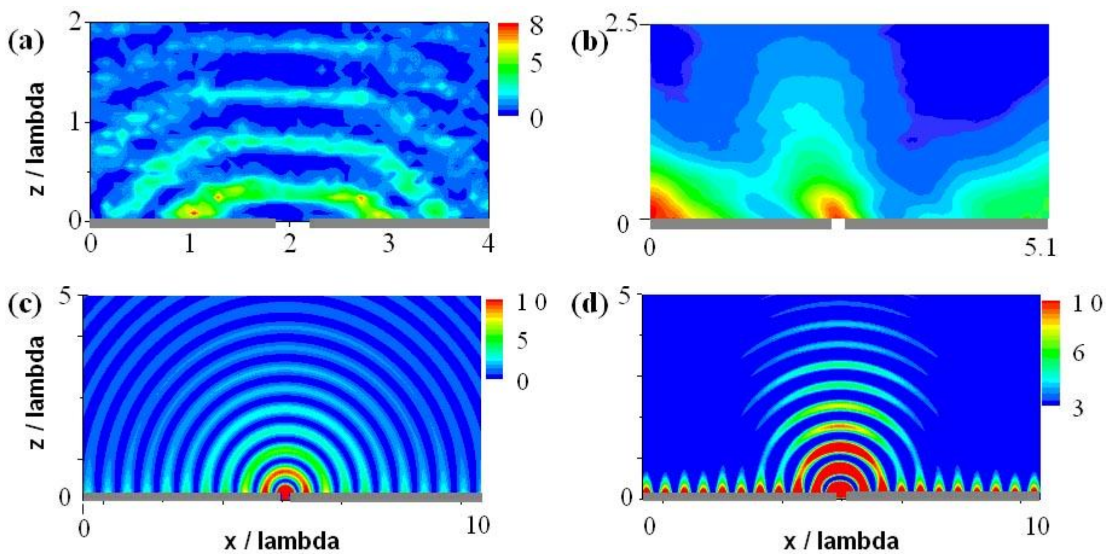

Fig. 3. Experimental and theoretical near-field images of the diffraction from a single slit aperture. (a) An experimentally measured near-field image at chosen frequency of 1.2 THz and slit width 60 μm. (b) An experimental near-field image at wavelength 780 nm and slit width 200 nm. (c) Theoretically calculated near-field images of a single slit diffraction from perfect conductor. (d) Same as (c), except for using a real conductor parameter of gold at wavelength of 780 nm.

The reason for the separation of SPP from space wave in optical frequency is due to a finite conductivity of metal: $|\varepsilon|$ is in range of 10-20. In contrast, metals in THz frequency act as perfect conductor, with the real part of the ε in order of 10^4, and the imaginary part in order of 10^5. Following the dispersion relation of SPP, SPP generated on a metal with such a large ε is very akin to the propagating light in free space. As a result, it is widely accepted that SPP in THz frequency regime is not a useful concept, as the 2D raster scanned images of experimental and theoretical results in fig. 3 show. Here, an interesting question arises: *from what ε value, can we be free of the SPP concept and consider the metal as perfect?* To investigate this problem systematically, we perform finite-difference-time-domain (FDTD) simulation in wide frequency range between optical and THz frequencies. The model structure is a single slit aperture perforated on a gold metal film, with the slit width scaled with the wavelength.

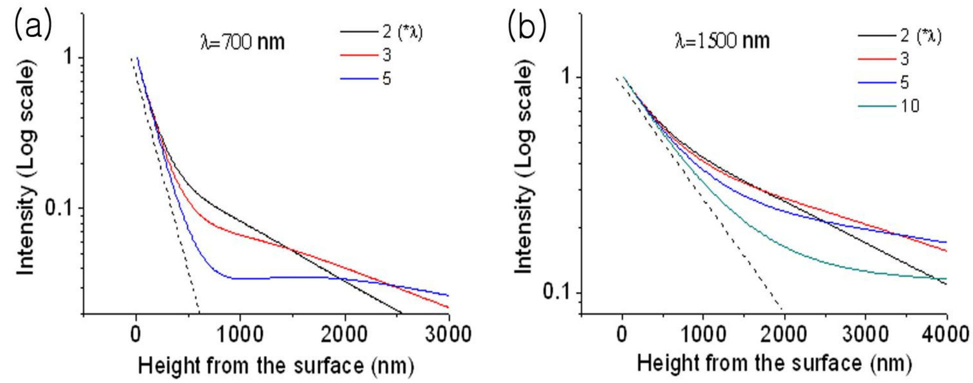

Fig. 4. FDTD results of the height dependent intensity at various distances away from the slit aperture along x-axis. (a) Height dependent plot with incident beam wavelength of 700 nm. (b) Height dependent near-field plot with incident beam wavelength of 1.5 μm. (dash) log plot of single exponentially decaying SPP.

We investigate the height dependent electric field intensity at various x-positions from the slit. SPP can be discriminated from space wave by their z-axis decay lengths, because SPP has its characteristic exponential decay length determined by metal permittivity while space wave doesn't. FDTD results show that whether we can distinguish SPP from space wave, and vice versa, is determined by two factors: the wavelength and the distance from the slit aperture. As shown in fig. 4(a), the height dependence shows a single exponentially decaying curve only close to the surface when the detecting position is at the distance of one wavelength away from the slit: SPP is buried into space wave. As we move farther away from the slit, the single exponentially decaying behavior begins to show up at a higher height, and it survives over a SPP decay length at a distance of five wavelengths from the slit. In contrast to 700 nm wavelength case, the height dependent curves slowly approach the single exponentially decaying curve (dash), and it should move over 10 wavelengths away from the slit to make SPP decaying curve survive over its characteristic decay length when the incident wavelength is 3 μm, as shown in fig. 4(b).

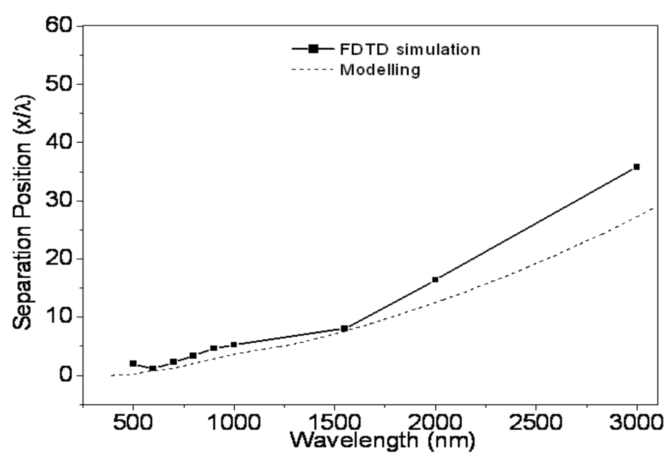

Fig. 5. Incident wavelength dependent SPP discrimination position defined as a distance along x-axis away from the slit aperture, where SPP begins to be discriminated from space wave.

To evaluate the SPP separation positions where SPP begins to be distinguished from space wave, we define the criteria for SPP separation as follows: SPP is considered separated from space wave when the initial decay behavior follows that of SPP. Shown in fig. 5 is the SPP separation position evaluated from FDTD simulations. This result is consistent with our expectation that a longer incident wavelength requires a farther SPP detecting position away from the slit to discriminate SPP from space wave.

We model the SPP separation from space wave in a single slit aperture by using a semi-analytic solution with the surface impedance boundary condition[8]. The z-axis polarized electric field of the diffracted light from a single slit aperture in real metal case with permittivity ε is written as

$$E_z(x,z) \sim \int_{-\infty}^{\infty} \frac{k_x}{\sqrt{k_0^2 - k_x^2} + k_0 W} \exp i(k_x x + \sqrt{k_0^2 - k_x^2}\, z) \quad dk_x, \tag{4}$$

where the surface impedance W is defined as $(1+\varepsilon)^{-1/2}$ and k_0 denotes the momentum vector of the incident light. Keeping only the non-evanescent terms, we arrive at the following approximation for space wave intensity at (x, z), with the slit aperture located at (0, 0):

$$I_{z,space} = | A_{space} \frac{x}{z + W\sqrt{x^2 + z^2}} (x^2 + z^2)^{-1/2} |^2 . \tag{5}$$

For a small W, Eq. (5) is dominated by space wave contributions in all regions of interest. Therefore, we can derive the criteria for having significant SPP features as $\delta_z = | W\sqrt{x^2 + \delta_z^{\,2}} |$, where δ_z is the evanescent decay length of SPP. Equivalently, the separation position is given by $x_d = \varepsilon\lambda / 4\pi$. The trend of the SPP separation from space wave is well appreciated by a plane wave expansion of the analytic solution. However, we note the limitation of our approximation. The SPP generation efficiency is an important factor in determining the SPP separation position. The wavelength dependency of SPP generation efficiency is known to be proportional to $1/\sqrt{\varepsilon(\lambda)}$ [9], showing a drastic decrease as the wavelength gets longer. Therefore, we need to include the SPP generation efficiency in our model, which is valid not only in optical frequency but also in longer wavelength regime.

4. CONCLUSIONS

In conclusion, we experimentally measure the diffracted light from subwavelength single slits both in optical and THz frequency regimes. SPP in optical frequency regime is well discriminated from space wave, while it is not in THz frequency regime. Based on FDTD simulations, we reveal that as wavelength becomes longer and therefore dielectric constant larger, the SPP separation position becomes farther and farther away from the slit. Finally in THz regime, the separation position is in order of meters, which is not realistically detectable. We believe our result will be beneficial to SPP application engineering in various wavelengths.

REFERENCES

[1] K. A. Norton, “The Physical Reality of Space and Surface Waves in the Radiation Field of Radio Antennas,” Proceedings of the Institute of Radio Engineers. **25**, 1192 (1937).

[2] Nicholas Fang, Hyesog Lee, Cheng Sun, and Xiang Zhang, “Sub=diffraction-limited optical imaging with a silver superlens,” Science 308, 534 (2005).

[3] Anthony Grbic, Lei Jiang, and Roberto Merlin, “Near-field plates: subdiffraction focusing with patterned surfaces,” Science 320, 511 (2008).

[4] Seunchul Kim, Jonghan Jin, Young-jin Kim, In-young Park, Yunseok Kim, and Seung-woo Kim, “High-harmonic generation by resonant plasmon field enhancement,” Nature 453, 757 (2008).

[5] J. B. Pendry, L. Martin-Moreno, F. J. Garcia-Vidal, “Mimicking surface plasmons with structured surfaces,” Science 305, 847 (2004).

[6] M. A. Seo, A. J. L. Adam, J. H. Kang, J. W. Lee, S. C. Jeoung, Q. H. Park, P. C. M. Planken, and D. S. Kim, "Fourier-transform terahertz near-field imaging of one-dimensional slit arrays: mapping of electric-field-, magnetic-field-, and Poynting vectors," Opt. Express **15,** 11781 (2007).

[7] K. G. Lee, H. W. Kihm, J. E. Kihm, W. J. Choi, H. Kim, C. Ropers, D. J. Park, Y. C. Yoon, S. B. Choi, D. H. Woo, J. Kim, B. Lee, Q. H. Park, C. Lienau, and D. S. Kim, "Vector field microscopic imaging of light," Nature Photonics **1,** 53-56 (2007).

[8] F. Lopez-Tejeira, F. J. Garcia-Vidal, and L. Martin-Moreno, "Scattering of surface plasmon by one-dimensional periodic nanoindented surfaces," Phys. Rev. B **72**, 161405 (2005).

[9] P. Lalanne, J. P. Hugonin, and J. C. Rodier, "Theory of Surface Plasmon Generation at Nanoslit Apertures," Phys. Rev. Lett. **95**, 263902 (2005).